

An Optical Intelligent Reflecting Surface-Assisted Underwater Wireless Communication System

REHANA SALAM¹, ANAND SRIVASTAVA¹ (Member, IEEE),
VIVEK ASHOK BOHARA¹ (Senior Member, IEEE), AND ASHWIN ASHOK² (Senior Member, IEEE)

¹Department of Electronics and Communications Engineering, Indraprastha Institute of Information Technology Delhi, New Delhi 110020, India

²Department of Computer Science, Georgia State University, Atlanta, GA 30303, USA

CORRESPONDING AUTHOR: R. SALAM (e-mail: rehanas@iiitd.ac.in)

ABSTRACT Optical intelligent reflecting surfaces (OIRS) have the potential to enhance the capacity of the next generation optical wireless communication systems by re-configuring the propagation environment of optical waves. In this work, a submerged OIRS and a planar mirror surface (PMS) are used to build up a non-line of sight (NLOS) underwater wireless optical communication (UWOC) system. An NLOS UWOC setup, which makes use of the total internal reflection (TIR) phenomenon, serves as a benchmark against which the OIRS/PMS-assisted UWOC systems are compared. With the help of the Mellin inverse transform, Meijer's G function, and Fox's H-function, the closed-form expressions for the probability density function (PDF), cumulative distribution function (CDF), average spectral efficiency (SE), average energy efficiency (EE), outage probability, and average bit error rate (BER) of the proposed systems are derived. Further, an asymptotic analysis of average SE is performed to illustrate a better understanding of these proposed system's performance at high SNR. The simulation results indicate that the OIRS-assisted UWOC system shows improved performance in comparison to benchmark scenario. Additionally, the efficient zones of OIRS deployment are analyzed.

INDEX TERMS UWOC, NLOS communication, OIRS, TIR, oceanic turbulence, visible light communications (VLC), exponential and generalized gamma (EGG) distribution, smart radio environment.

I. INTRODUCTION

HUMAN interest in oceanographic research, offshore oil exploration, disaster prevention, unmanned operations, seafloor mapping, and monitoring has considerably grown [1]. Consequently, reliable and high throughput underwater wireless communication (UWC) networks are required. Optical communication is one way to cater to the high data rate demand. The conventional radio frequency (RF) based UWC suffers from significant amount of attenuation, whereas acoustic based UWC has significant delays and low data rates. Four distinct underwater wireless optical communication setups described in the literature for data transmission are, point-to-point (P2P) line of sight (LOS) configuration, diffused LOS configuration, retro reflector-based LOS configuration, and non-line of sight (NLOS) configuration [2]. P2P LOS setup uses a light source, i.e., LASER, with a small divergence angle and LOS

communication between the transmitter and the receiver. In this setup, precise pointing between the transmitter and receiver is necessary [3]. In a diffused LOS configuration, a light source with a large divergence angle is used. It is a type of broadcasting underwater wireless optical communication (UWOC) system in which information is passed from one node to many nodes. The need for exact pointing between the transmitter and receiver is not required in this situation. Small communication distances and low data rates are the disadvantages of this configuration [3]. Retro reflector-based LOS configuration is a special case of P2P LOS configuration and is suitable for duplex UWOC systems. In this configuration, the transmitted light is reflected back from a retro-reflector. The advantages include reduced volume, weight, and power consumption of transceivers. One of the serious flaws in this setup is backscattering. An NLOS-UWOC configuration can be used when the direct LOS communication between the

transmitter and the receiver is blocked. The NLOS configuration is based on the total internal reflection (TIR) principle. In this setup, the signal is transmitted towards the water-air interface, which is partially refracted and partially reflected at interfaces between the mediums with different refractive indices. The reflected signal is relayed to the receiver (facing the sea surface) [2]. So the NLOS arrangement overcomes the LOS UWOC alignment constraint. One of the challenges of this configuration is the varying sea surface slopes [3]. The authors in [4] investigated the LOS and NLOS models in an underwater sensor network taking into account the channel characteristics and the communication system parameters for the NLOS UWOC configuration. The authors in [5] studied and analyzed vertical linkages for underwater visible light communication (UWVLC) while taking underwater environment heterogeneity into account. In [6], the authors examined parameter optimization for an underwater optical wireless vertical link that is vulnerable to link misalignment due to the slopes of the sea surface. Based on experimental data, Zedini et al. proposed a unified statistical model in [7] to describe turbulence-induced fading in UWOC systems. Rahman et al. investigated the generalized Gamma (GG), exponential and generalized Gamma (EGG), Exponentiated Weibull (EW), and Gamma-Gamma ($\Gamma\Gamma$) turbulence models for a mixed terrestrial wireless optical communication-UWOC (TWOC-UWOC) system with multilayer UWOC channel in [8]. In [9], Huang et al. extended the underwater light transmission distance to 6 m by using reflective mirrors inside a water tank.

Intelligent reflecting surface (IRS) is a revolutionary technology to improve the performance of wireless communication systems by creating intelligent and reconfigurable wireless channels and radio propagation environments for beyond fifth-generation (B5G) and sixth-generation (6G) communication networks [10]. In RF, a significant number of small reflecting elements are collectively adjusted to reconfigure the wireless signal transmission environment. These numerous inexpensive passive reflecting elements (also referred as meta-atoms or lattices) have the ability to independently adjust the reflection coefficients, that is, the amplitude and/or phase shift of the incident signal, and passively reflect it to the desired direction [11]. This method addresses the need for a smart radio environment (SRE), in which the radio propagation environment is transformed into an intelligent reconfigurable space that is crucial for transmitting radio signals from the transmitter to the intended receiver without producing new radio signals and thereby without incurring any further power consumption [12]. SRE is enabled by IRS which is often made of thin material and can be easily attached to indoor surfaces, including walls, ceilings, and buildings.

Mirror-based optical IRS and meta-surface-based optical IRS are the two different forms of optical intelligent reflecting surfaces (OIRS) [13]. Mirrors and other reflecting elements have long been actively used in optical

systems. According to the application, small mirror elements with sizes ranging from many hundreds of micrometers to centimeters make up the mirror-based OIRS, which are also known as deformable mirrors. Micro-electro-mechanical systems (MEMS) enable their repositioning and reorientation [11]. A discrete planar array of subwavelength unit cells make up meta-surface-based OIRS, which can modify reflected wave properties like phase, amplitude, and polarisation. Though conceptually similar to RF meta-surfaces [11], optical meta-surfaces are realized at optical frequencies using nanoscale technologies that are very different from the conventional antenna technologies used in the RF band. In [14], Aboagye et al. used an OIRS in the indoor environment and evaluated the performance in terms of data rate and outage, considering the receiver's orientation. The authors of [15] have described performance improvement by dynamically changing the wireless channels with the aid of an IRS. The authors in [16] analyzed the position of IRS in multi-user multiple input multiple outputs (MIMO) systems, where IRS is used to facilitate data transmission for both uplink as well as downlink phases. The authors in [17] utilized an OIRS to develop a configurable wireless indoor environment to improve the physical layer security. In order to relax the LOS constraint for free space optical (FSO) systems, the authors in [18] investigated the effect of OIRS's physical characteristics, such as its size, location, and orientation, on the performance of the end-to-end FSO channel. The average energy efficiency (EE) and transmission power needed for an IRS-assisted system and decode and forward (DF) relay-assisted systems are examined in [19]. Similar to [19], the authors in [20] compared an IRS-assisted system to a full-duplex (FD) DF relay-assisted system with hardware impairments.

A. RELATED WORKS

1) MIXED TERRESTRIAL-UWOC SYSTEMS

In [21], Yang et al. have considered a mixed FSO-UWOC dual-hop transmission system considering both heterodyne detection and intensity modulation with direct detection (IM/DD). They assumed $\Gamma\Gamma$ fading for the FSO channel and EGG fading with pointing errors for the UWOC channel and derived the closed-form expressions for the outage probability, average bit error rate, and average capacity in terms of the bivariate Fox's H-function. In [22], the authors analyzed the outage probability, average bit error rate (BER), and ergodic capacity for various types of waters (fresh water, salty water) utilizing an RF-IRS in the terrestrial link for a mixed RF-UWOC system. In [23], the authors investigated the performance of triple hop IRS-assisted RF-FSO UWOC system considering Nakagami-m fading channel over the IRS-RF link and the $\Gamma\Gamma$ over the IRS-FSO and UWOC links. The performance is evaluated in terms of the average BER and outage probability. Further, in [24], the performance of a NOMA-based IRS-assisted hybrid RF-UWOC system is explored.

2) COMPLETELY UWC SYSTEMS

The authors in [25] presented an underwater optical wireless sensor network (UOWSN) to monitor and discover ore deposits in continental margin regions. The outage probability and average BER of the proposed system is computed while considering turbulence and misalignment. As a cluster head, a DF relay acts as a mediator for communication between the source nodes and receiver. In [26], the authors studied the potential network architecture for an underwater Internet of Things (IoT), and IRS is identified as one of the promising techniques for aiding underwater IoT. The authors explained the benefits of implementing IRS in challenging environments (CEs) such as underwater, underground, industrial, and disaster environments in which signal propagation and connectivity using traditional signaling technologies are easily impaired in [27]. IRS's potential use cases, deployment strategies, and design aspects are examined in the context of underwater IoT, underground IoT, industry, and emerging networks. The authors employed an acoustic IRS to improve the performance of an underwater communication system. It has been demonstrated that the performance of all CEs improves with an increase in the number of reflecting elements of the IRS. Furthermore, the idea of acoustic beamforming using specially constructed meta-surfaces is investigated in [28]. In [29], Sun et al. presented a new hardware solution based on a reconfigurable array of piezoelectric reflectors for constructing an acoustic IRS in order to achieve high data rates and long communication range underwater. To limit the effects of sea currents, an extended Kalman filter (EKF)-based algorithm is developed. According to the findings, the data rate varies from 2 kbps for no IRS case to hundreds of kbps when utilizing an IRS. In [30], the authors studied an IRS-assisted UWOC system employing a meta-surface based OIRS while accounting for underwater turbulence, beam attenuation, occlusion or blockage due to objects, and beam direction errors. Underwater turbulence is modelled using GG turbulence model. Outage probability, BER, and channel capacity are used to analyze system performance. The effect of changing channel characteristics and the blocking probability coefficient is investigated, and the results show enhanced system performance with an increase in the number of IRS elements. Furthermore, in [31], the authors utilized the recently developed Oceanic Turbulence Optical Power Spectrum (OTOPS) model to characterize the underwater turbulent medium. The impacts of the turbulent medium are considered along with the parameters of the communication system (such as communication range, receiver aperture diameter, and number of IRS elements) in the numerical findings that are presented. It is demonstrated that IRS can significantly improve the reliability of UWOC systems under the impacts of attenuation, beam displacement, and turbulence.

As stated above, there is a substantial amount of literature available on the performance of IRS-assisted UWOC systems where the IRS is positioned in the system's terrestrial

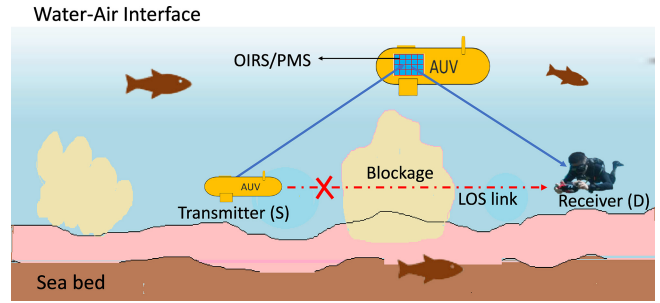


FIGURE 1. Illustration of the OIRS/PMS-aided UWOC system.

link. However, there is dearth of work in the literature that uses a submerged OIRS. Furthermore, submerged mirror-based OIRS and planar mirror surface (PMS) for UWOC has not yet been explored. As a result, the performance of a submerged mirror-based OIRS and PMS-assisted UWOC systems are investigated in this paper.

B. MOTIVATION AND CONTRIBUTIONS

To the best of the author's knowledge, the proposed research work is first of its kind to propose a technique for UWOC employing mirror array based OIRS and PMS. For NLOS UWOC, we can use both mirror based OIRSs and meta-surface based OIRSs. However, according to the findings in [32], the mirror array outperforms the meta-surface in a visible light communication (VLC) system. As a result, we assume OIRS to be an intelligent controllable mirror array in the proposed work. An OIRS/PMS is placed on a submerged autonomous unmanned vehicle (AUV) to facilitate communication between transmitter and receiver, when direct LOS communication is not feasible. The basic conceptual diagram is illustrated in Fig. 1. The conventional NLOS UWOC configuration, which operates on the TIR principle, can also be utilized, but only in cases where the UWOC system is needed to work close to the water's surface (air-water interface), as optical signals have limited transmission range. Moreover, the performance of the NLOS system is negatively impacted by sea surface slopes. OIRS/PMS-assisted UWOC systems have the advantage of being installed at any depth from the water-air interface (depending upon the application) to circumvent this problem.

In light of above, the main contributions of this paper can be summarized as follows:

- 1) An OIRS and PMS-assisted UWOC system is analyzed for underwater communication between the transmitter and receiver and compared with conventional NLOS UWOC configuration, taking into account underwater attenuation and turbulence effects.

- 2) Utilizing Meijer's G function and the bivariate Fox's H-function, generalized closed-form analytical expression for the probability density function (PDF), cumulative distribution function (CDF), average spectral efficiency (SE), average EE, outage probability, and average BER of the OIRS, PMS, and NLOS-assisted UWOC systems are derived.

TABLE 1. Main notations and definitions.

Notation	Definitions
$\mathbb{E}[\cdot]$	Expectation operator
γ	Instantaneous SNR
$\bar{\gamma}$	Average SNR
ω, λ, a, b, c	EGG Distribution parameters
$G_{p,q}^{m,n} \left(z \mid \begin{matrix} (a_k)_{k=1}^p \\ (b_k)_{k=1}^q \end{matrix} \right)$	Meijer's G function
$H_{p,q}^{m,n} \left(z \mid \begin{matrix} (a_k)_{k=1}^p \\ (b_k)_{k=1}^q \end{matrix} \right)$	Fox's H function
$\psi(x) = \frac{d}{dx} \ln \Gamma(x)$	Psi function
σ_I^2	Scintillation index
(x_s, y_s, z_s)	Coordinates of transmitter
(x_d, y_d, z_d)	Coordinates of receiver
(x_{kl}, y_{kl}, z_{kl})	Coordinates of OIRS
Φ	Irradiance angles
ψ	Incidence angles
θ_i	angles of incidence
θ_t	angle of transmission
θ_r	angle of reflection
$\theta = \theta_i$	For smooth water-air interface
d_{sr}	distance from S to OIRS/PMS
d_{rd}	distance from OIRS/PMS to D

To verify the derived expressions and to demonstrate the performance of OIRS and PMS-assisted UWOC system for different parameters of interest, numerical and simulation analysis are used. All analytical expressions are corroborated through Monte Carlo simulation.

3) Furthermore, an asymptotic analysis for SE in the high SNR regime is derived to illustrate the effect of channel parameters on the performance of the investigated system. The asymptotic results at high SNR regime are found to be accurate since the asymptotic expression of the average SE at high SNR completely matches the analytical expression.

4) In addition, the efficient zones of OIRS deployment for UWOC systems under EGG distributed fading channel are analyzed. It is shown that in OIRS-aided UWOC systems, deployment of OIRS close to the transmitter or the receiver always show worse performance than its far deployments.

C. ORGANIZATION AND NOTATIONS

The structure of the paper is as follows. The system models for each of the three UWOC scenarios have been briefly discussed in Section II. The various performance metrics, such as average SE, average EE, outage probability, and average BER, have been evaluated in Section III. The numerical and simulation analysis of the proposed system model are presented in Section IV. In Section V, important conclusions and suggestions for further work are presented. Table 1 contains a list of the key notations used in the manuscript.

II. SYSTEM MODEL

Due to obstructions and dynamic nature of the water, LOS communication in underwater is rarely possible. NLOS based communication is, therefore, a preferred option. Fig. 1 illustrates the system model for the OIRS and PMS scenarios for a static UWOC system in pure seawater.

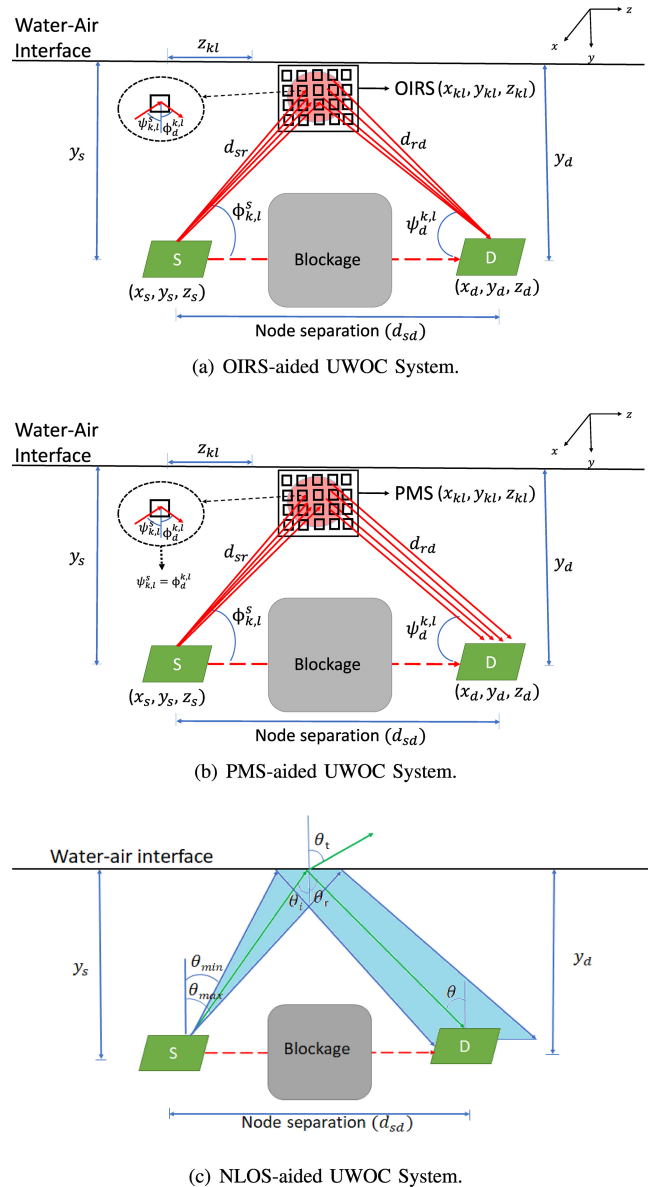


FIGURE 2. 3D-coordinate system model.

Fig. 2(a) and 2(b) shows the 3D-coordinate model for the OIRS-aided UWOC system and PMS-aided UWOC respectively, in which a single AUV serves as the transmitter for the entire communication system. A planar OIRS/PMS is mounted on another AUV that is in direct LOS with the transmitter and receiver. It is assumed that the communication between the transmitter and receiver occurs via OIRS/PMS as the direct LOS communication is blocked. Multiple mirror elements make up the mirror-based OIRS/PMS. The OIRS receives the signal from the transmitter and forwards it in the desired direction by changing the orientation of each OIRS element. A mechanical steering gear individually rotates each unit's lens-coated surface material [11]. The beam can be focused to a certain location where the size of the target spot is correlated with the size of the mirror unit by adjusting the deflection direction of each mirror unit. The optical signal is

not altered in terms of phase, amplitude, or other properties by the mirror type OIRS. However, signal re-transmission in the PMS situation follows the straight forward Snell's law. The PMS is comparable to the OIRS, with the exception that each element in the PMS is fixed and cannot be oriented. This work assumes that the total number of reflecting elements (n_m^2) in OIRS and PMS are same. Further, it is assumed that the AUV with OIRS/PMS is situated just below sea surface to ensure that the entire system is submerged. In order to keep the system analytically tractable, it is also assumed that these underwater devices are stationary and ocean currents and sea surface slopes have minimal impact on them.

Fig. 2(c) shows the 3D-coordinate model of NLOS-aided UWOC system in which the transmitted signal is reflected towards the receiver from the smooth water-air interface (Here, no OIRS or PMS is used to reflect the signal). In this scenario, the water-air interface behaves as a perfect mirror [4] when the incident angle is greater than the critical angle, and the signal is reflected into the same medium toward the receiver according to the TIR phenomenon.

A. CHANNEL MODEL

In the considered setup, a light-emitting diode (LED) is employed at the transmitter and a high-sensitivity photodetector (PD), i.e., a silicon photomultiplier (SiPM), which consists of an array of single-photon avalanche diodes (SPADs), at the receiver. The transmitter and receiver are separated by node separation distance represented as d_{sd} . The OIRS controller is assumed to be aware of the channel state information (CSI). The transmitter is positioned at a depth of y_s from the air-water interface, and the link geometry is depicted in Fig. 2. The distance of the receiver from the air-water interface is denoted as y_d . Transmitted signal x from the AUV transmitter having power of P_t is reflected by the OIRS/PMS to the intended receiver. Thus the received signal at the receiver is represented as [6], [8]

$$y = G_i h_p h_\alpha x + \Omega_i, \quad (1)$$

where G_i ($i \in \{O, P, N\}$), stands for the corresponding OIRS, PMS, and NLOS-assisted UWOC system channel gains respectively, and which accounts for the spread of the transmitted beam between the transmitter and receiver, h_p is the attenuation loss, h_α models the underwater turbulence effect, and Ω_i is the additive white Gaussian noise (AWGN) with variance $\sigma_{\Omega_i}^2$, which comprises of shot noise, dark current noise, background noise, and thermal noise and is given as [6]

$$\sigma_{\Omega_i}^2 = \sigma_{sh,i}^2 + \sigma_d^2 + \sigma_b^2 + \sigma_{th}^2, \quad (2)$$

where $\sigma_{sh,i}^2 = 2eGFBI_{s,i}$, $\sigma_d^2 = 2eGFBI_d$, and $\sigma_{th}^2 = \frac{4K_B T B}{R_L}$ denotes the variances of the signal shot noise, dark noise and thermal noise, respectively, wherein e , G , K_B , T , F , B and R_L denote the electron charge, SiPM gain, Boltzmann constant, the receiver equivalent temperature in kelvin, the PD excess

noise factor, the bandwidth of the receiver's lowpass filter (LPF), and the load resistance, respectively. Also, I_d represent the SiPM dark current and $I_{s,i} = \mathcal{R}_e G_i h_p h_\alpha$ represent the useful signal, wherein \mathcal{R}_e is the SiPM responsivity. For the sake of simplicity, the impact of solar radiation background noise is ignored; thus, the variance of background noise (σ_b^2) = 0 [6].

By continuously reducing the total propagation energy of an emitting light beam, absorption limits the transmission range of an UWOC link. In contrast, scattering disperses the photons in a random direction, causing some of them to escape the receiver's finite aperture while others may be delayed in reaching it because they followed various propagation paths. As a result, scattering causes time jitter, inter-symbol interference, and multi-path fading effects. The attenuation loss (h_p) depends on the type of water and is modeled using the well-known Beer-Lambert's law as [2]

$$h_p = e^{-c(\lambda)(d_{sr}+d_{rd})}, \quad (3)$$

where d_{sr} is the distance from the source to the centroid of OIRS/PMS, d_{rd} is the distance from OIRS/PMS to the receiver, and $c(\lambda)$ is the wavelength-dependent attenuation coefficient and it is the summation of the absorption coefficient $a(\lambda)$ and scattering coefficient $b(\lambda)$. The concentration of chlorophyll (C_c) is the key determinant of absorption, which is the most important component in optical beam attenuation in UWOC. C_c is typically used to classify different water types [31].

Using a mixture of EGG distributions, the seawater turbulence can be represented as [7]

$$h_\alpha(\alpha) = \omega f(\alpha; \lambda) + (1 - \omega)g(\alpha; [a, b, c]), \quad (4)$$

with

$$f(\alpha; \lambda) = \frac{1}{\lambda} \exp\left(-\frac{\alpha}{\lambda}\right),$$

$$g(\alpha; [a, b, c]) = c \frac{\alpha^{ac-1} \exp\left(-\left(\frac{\alpha}{b}\right)^c\right)}{b^{ac} \Gamma(a)},$$

where f and g denote the exponential and generalized Gamma distributions, respectively, ω is the mixture weight or mixture coefficient of the distributions, satisfying $0 < \omega < 1$, λ is the parameter associated with the exponential distribution, a , b and c are the parameters of the generalized Gamma distribution, and $\Gamma(\cdot)$ denotes the Gamma function.

1) OIRS CHANNEL GAIN

In the proposed framework, OIRS consists of $n_m \times n_m$ mirror elements. The dimension of each element is $l_m \times w_m$, where l_m and w_m represent the length and width of an individual mirror element, respectively. The channel gain of the reflected signal from each of the OIRS elements in the k^{th} row and l^{th} column is given as [14], [32]

$$G_{O_{k,l}}(\beta, \Gamma) = \begin{cases} \frac{\rho \eta (m+1) \text{APD}}{2\pi (d_{sr}+d_{rd})^2} C_1 C_2 C_3 C_4 T(\psi) G(\psi), & 0 \leq \psi_d^{k,l} \leq \psi_{F0V} \\ 0, & \text{otherwise,} \end{cases} \quad (5)$$

where ρ is the reflection coefficient of the OIRS element, η is the current-to-light conversion efficiency of the LED, A_{PD} is the area of the photo diode, m represents the Lambertian order which is given by $m = -\ln(2)/\ln(\cos(\Phi_{1/2}))$, where $\Phi_{1/2}$ is LED semi angle. Further, $C_1 = \cos^m(\Phi_{k,l}^s)$ where $\Phi_{k,l}^s$ is the angle of irradiance from the transmitter to OIRS. Likewise, $C_2 = \cos(\psi_{k,l}^s)$ with $\psi_{k,l}^s$ being the angle of incidence on the OIRS, $C_3 = \cos(\Phi_d^{k,l})$ with $\Phi_d^{k,l}$ being the angle of irradiance from the k^{th} row and l^{th} column OIRS element towards the receiver and $C_4 = \cos(\psi_d^{k,l})$ with $\psi_d^{k,l}$ being the angle of incidence at the receiver. The gains of the optical filter and non-imaging concentrator are $T(\psi)$ and $G(\psi)$, respectively, and the field of view (FoV) of the receiver is ψ_{FoV} . The concentrator gain can be expressed as $G(\psi) = \mu^2 / \sin^2 \psi_{FoV}$, $0 \leq \psi \leq \psi_{FoV}$, where μ is the refractive index. The cosine of the angle of irradiance (which is specified by the yaw and roll angles of the mirror array) can be expressed as [14]

$$\cos(\Phi_d^{k,l}) = \frac{(x_{k,l} - x_d)}{d_{rd}} \sin(\beta) \cos(\Gamma) + \frac{(y_{k,l} - y_d)}{d_{rd}} \cos(\beta) \cos(\Gamma) + \frac{(z_{k,l} - z_d)}{d_{rd}} \sin(\Gamma), \quad (6)$$

where $(x_{k,l}, y_{k,l}, z_{k,l})$ and (x_d, y_d, z_d) denote the position vectors specifying the locations of the OIRS and the receiver, respectively. The mirror orientation is obtained by finding a unit vector normal to its surface, $\hat{\mathbf{N}}_{k,l}$ which can be expressed as [32]

$$\hat{\mathbf{N}}_{k,l} = \frac{\widehat{\mathbf{R}}_{k,l} \mathbf{S} + \widehat{\mathbf{R}}_{k,l} \mathbf{D}}{\sqrt{2 + 2\widehat{\mathbf{R}}_{k,l} \mathbf{S}^T \widehat{\mathbf{R}}_{k,l} \mathbf{D}}}, \quad (7)$$

where the $\widehat{\mathbf{R}}_{k,l} \mathbf{S}$ represents the corresponding incidence direction and $\widehat{\mathbf{R}}_{k,l} \mathbf{D}$ represents the reflection direction. Moreover, \mathbf{S} , $\mathbf{R}_{k,l}$ and \mathbf{D} stand for the source coordinates of the source's centre, the centroid coordinates of the mirror in k^{th} row and l^{th} column, respectively, and the destination coordinates. The vectors \mathbf{S} , $\mathbf{R}_{k,l}$ and \mathbf{D} are given as

$$\mathbf{S} = \begin{bmatrix} -(x_s + \frac{w_m}{2} + (l-1)w_m) \\ y_s \\ -(z_s + \frac{l_m}{2} + (k-1)l_m) \end{bmatrix},$$

$$\mathbf{R}_{k,l} = \begin{bmatrix} (x_s + \frac{w_m}{2} + (l-1)w_m) \\ 0 \\ (z_s + \frac{l_m}{2} + (k-1)l_m) \end{bmatrix},$$

$$\mathbf{D} = \begin{bmatrix} x_d - (x_s + \frac{w_m}{2} + (l-1)w_m) \\ y_d \\ z_d - (z_s + \frac{l_m}{2} + (k-1)l_m) \end{bmatrix}.$$

Furthermore, the rotation angles can be computed using the obtained normal vector $\hat{\mathbf{N}}_{k,l}$ as

$$\beta_{k,l} = \sin^{-1}(\hat{\mathbf{N}}_{k,l}^T \mathbf{e}_3), \quad (8)$$

and

$$\Gamma_{k,l} = \sin^{-1}(\hat{\mathbf{N}}_{k,l}^T \mathbf{e}_1 / \cos(\beta_{k,l})), \quad (9)$$

where \mathbf{e}_c ($c \in \{1, 2, 3\}$) represents the c^{th} column of a 3×3 identity matrix.

From (3), (4), and (5), the total path loss (DC gain) for an $n_m \times n_m$ square OIRS-assisted underwater channel is given as [14]

$$H_{OIRS} = \sum_{k=1}^{n_m} \sum_{l=1}^{n_m} G_{O_{k,l}}(\beta, \Gamma) h_p h_\alpha. \quad (10)$$

Assuming a point light source, and the distance of light transmission to be sufficiently large as compared to the size of the light source and small OIRS dimensions, (10) can be approximated as [32]

$$H_{OIRS} \approx n_m^2 G_{O_{k,l}}(\beta, \Gamma) h_p h_\alpha. \quad (11)$$

Therefore, the overall received power can be given as

$$P_R = \mathcal{R}_e P_t H_{OIRS}, \quad (12)$$

where P_t is the total transmit power, \mathcal{R}_e is the SiPM responsivity which is given as [6]

$$\mathcal{R}_e = \left(\frac{\Upsilon_{PDE}}{E_{ph}} \right) (1 + P_{AP} + P_{CT}) eG.$$

Here, E_{ph} is the photon energy, G , Υ_{PDE} , P_{AP} , and P_{CT} , denote the SiPM gain, the photon detection efficiency, the probability of after-pulsing, and the probability of crosstalk, respectively. A detailed description of SiPM parameters can be found in [33] and [34].

2) PMS CHANNEL GAIN

The channel gain for PMS-assisted UWOC system is given as

$$G_{P_{k,l}} = \begin{cases} \frac{\rho \eta (m+1) A_{PD}}{2\pi (d_{sr} + d_{rd})^2} C_1 C_2 C_3 C_4 T(\psi) G(\psi), & 0 \leq \psi_d^{k,l} \leq \psi_{FoV} \\ 0, & \text{otherwise.} \end{cases} \quad (13)$$

Based on the geometrical layout depicted in Fig. 2(b), C_1, C_2, C_3 and C_4 are calculated as shown in (14) at the bottom of the next page.

Thus the total channel gain for a PMS assisted underwater channel is given as

$$H_{PMS} = \sum_{k=1}^{n_m} \sum_{l=1}^{n_m} G_{P_{k,l}} h_p h_\alpha. \quad (15)$$

Therefore, the total received optical power, P_R from all reflected paths at the receiver can be expressed as

$$P_R = \mathcal{R}_e P_t H_{PMS}. \quad (16)$$

3) NLOS CHANNEL GAIN

Fig. 2(c) provides an illustration of the NLOS-assisted UWOC system. In this system, the LED transmits a cone of light defined by an angle pair called θ_{\min} and θ_{\max} in the direction of the air-water contact/interface, which is reflected towards the underwater receiver obeying TIR.¹ The main condition for TIR is that the signal must be traveling from a denser medium to a rarer medium and the angle of incidence is greater than the critical angle. At TIR, the interface acts as a perfect mirror and reflects the whole of the light back into the same medium. The channel gain of the NLOS UWOC system can be expressed as [35]

$$G_N = \begin{cases} \frac{\eta A_{PD} \cos(\theta_i)}{2A_{\text{ann}}} \left[(R_s)^2 + (R_p)^2 \right], & \theta_{\min} \leq \theta_i \leq \theta_c \\ \frac{\eta A_{PD} \cos(\theta_i)}{2A_{\text{ann}}}, & \theta_c \leq \theta_i \leq \theta_{\max} \\ 0, & \text{otherwise,} \end{cases} \quad (17)$$

where the annular surface (A_{ann}) is given by [4]

$$A_{\text{ann}} = 2\pi(y_s + y_d)^2 [\cos(\theta_{\min}) - \cos(\theta_{\max})]. \quad (18)$$

Further, R_s is the s -polarised reflection coefficient, and R_p is the p -polarised reflection coefficient given in [36]

$$R_s = \left[\frac{\mu_w \cos(\theta_i) - \mu_a \cos(\theta_t)}{\mu_w \cos(\theta_i) + \mu_a \cos(\theta_t)} \right]^2 = \left[\frac{\sin(\theta_i - \theta_t)}{\sin(\theta_i + \theta_t)} \right]^2, \quad (19)$$

$$R_p = \left[\frac{\mu_w \cos(\theta_t) - \mu_a \cos(\theta_i)}{\mu_w \cos(\theta_t) + \mu_a \cos(\theta_i)} \right]^2 = \left[\frac{\tan(\theta_t - \theta_i)}{\tan(\theta_t + \theta_i)} \right]^2. \quad (20)$$

where θ_i and θ_t are the angles of incidence and transmission and μ_a is the refractive index of air and μ_w is the refractive index of water.

Polarized light propagating through an aquatic channel would lose its polarization properties due to the scattering nature of the medium. Hence it is assumed that the light reaching the water-air surface is totally unpolarized, and its reflectivity is given by $R = \frac{1}{2}(R_s + R_p)$. The overall channel gain, in this case, can be given as

$$H_{NLOS} = G_N h_p h_\alpha. \quad (21)$$

Accordingly, the received power can be expressed as [35]

$$P_r = \mathcal{R}_e P_t H_{NLOS} G(\psi) T(\psi). \quad (22)$$

1. The TIR phenomenon states that when the incidence angle is greater than the critical angle $\theta_c = \sin^{-1}(\frac{\mu_a}{\mu_w})$, the light is reflected back into the same medium (water) after illuminating an annular area at the sea surface.

B. STATISTICAL CHARACTERIZATION OF SNR

In this subsection, an EGG distribution-based statistical analysis for the turbulent underwater channel is developed. In the following Lemma, the PDF and CDF of the SNR for the OIRS/PMS-assisted UWOC system under the combined effect of underwater attenuation and turbulence is evaluated:

Lemma 1: Expressions for the PDF of seawater turbulent channel (h_α) is given as:

$$f_{h_\alpha}(h_\alpha) = \frac{\omega}{\alpha} H_{0,1}^{1,0} \left[\frac{\alpha}{\lambda} \mid (1, 1) \right] + \frac{(1-\omega)}{\alpha \Gamma(a)} H_{0,1}^{1,0} \left[\frac{\alpha}{b} \mid (a, 1/c) \right]. \quad (23)$$

Proof: See Appendix A. ■

Next, we use (23) to analyze the UWOC system performance. Assuming IM/DD technique and on-off keying (OOK) modulation with $x \in \{0, \sqrt{2P_t}\}$ and P_t as average transmitted optical power, therefore the instantaneous received electrical SNR is given as [6]

$$\gamma = \frac{\mathcal{R}_e^2 P_t^2 G_i^2 h_p^2 h_\alpha^2}{\sigma_{\Omega_i}^2} = \bar{\gamma} h_\alpha^2, \quad (24)$$

where $\bar{\gamma} = \frac{\mathcal{R}_e^2 P_t^2 G_i^2 h_p^2}{\sigma_{\Omega_i}^2}$ is the average electrical SNR. Then, applying the transformation of random variable $\gamma = \bar{\gamma} h_\alpha^2$, the PDF of SNR for the UWOC system under the effect of the seawater turbulence in terms of the Fox-H function can be expressed as

$$f_\gamma(\gamma) = \frac{\omega}{2\gamma} H_{0,1}^{1,0} \left[\frac{1}{\lambda} \sqrt{\frac{\gamma}{\bar{\gamma}}} \mid (1, 1) \right] + \frac{(1-\omega)}{2\gamma \Gamma(a)} H_{0,1}^{1,0} \left[\frac{1}{b} \sqrt{\frac{\gamma}{\bar{\gamma}}} \mid (a, 1/c) \right]. \quad (25)$$

Lemma 2: The CDF of SNR is derived in lemma 2 and is expressed in terms of Fox-H function as

$$F_\gamma(\gamma) = \omega H_{1,2}^{1,1} \left[\frac{1}{\lambda} \sqrt{\frac{\gamma}{\bar{\gamma}}} \mid (1, 1)(0, 1) \right] + \frac{(1-\omega)}{\Gamma(a)} H_{1,2}^{1,1} \left[\frac{1}{b} \sqrt{\frac{\gamma}{\bar{\gamma}}} \mid (a, 1/c)(0, 1) \right]. \quad (26)$$

Proof: See Appendix B. ■

III. PERFORMANCE ANALYSIS

In this section, derive the outage probability, average SE, average EE, and average BER results to investigate the proposed UWOC system performance is derived.

$$\begin{aligned} C_1 &= \cos^m(\Phi_{k,l}^s) = \frac{d_{sd}}{\sqrt{(d_{sd}^2 + (2y_s)^2)}}, C_2 = \cos(\psi_{k,l}^s) = \frac{y_d}{0.5 \times \sqrt{(d_{sd}^2 + (2y_d)^2)}}, \\ C_3 &= \cos(\Phi_d^{k,l}) = \frac{y_s}{0.5 \times \sqrt{(d_{sd}^2 + (2y_s)^2)}}, C_4 = \cos(\psi_d^{k,l}) = \frac{d_{sd}}{\sqrt{(d_{sd}^2 + (2y_d)^2)}} \end{aligned} \quad (14)$$

A. OUTAGE PROBABILITY

Outage probability is a performance metric that can be defined as the probability that the instantaneous SNR (γ) falls below a certain threshold (γ_{th}) and is mathematically expressed as

$$P_{out} = P(\gamma < \gamma_{th}) = F_{\gamma}(\gamma_{th}). \quad (27)$$

B. AVERAGE SPECTRAL EFFICIENCY

The average SE for the UWOC system is defined as [37]

$$\overline{SE} = \int_0^{\infty} \log_2(1 + \tau\gamma) f_{\gamma}(\gamma) d\gamma, \quad (28)$$

where $\tau = \frac{c}{2\pi}$ for IM/DD [38].

Using (25) and utilizing [39, eq. (8.4.6/5)], and then converting Meijer's G-function to FOX's H function as

$$\log_2(1 + \tau\gamma) = 1.44H_{2,2}^{1,2} \left[\tau\gamma \mid \begin{matrix} 1, 1 \\ 1, 0 \end{matrix} \right], \quad (29)$$

(28) can be expressed as

$$\begin{aligned} \overline{SE} = & 0.72\omega H_{p+2, q+3}^{m+3, n+1} \left[\frac{1}{\lambda} \sqrt{\frac{1}{\tau\gamma}} \mid \begin{matrix} (0, 1/2)(1, 1/2) \\ (1, 1)(0, 1/2)(0, 1/2) \end{matrix} \right] \\ & + 0.72 \frac{(1-\omega)}{\Gamma(a)} H_{p+2, q+3}^{m+3, n+1} \left[\frac{1}{b} \sqrt{\frac{\gamma}{\tau\gamma}} \mid \begin{matrix} (0, 1/2)(1, 1/2) \\ (a, 1/c)(0, 1/2)(0, 1/2) \end{matrix} \right]. \end{aligned} \quad (30)$$

An accurate, simple closed-form approximation of the average SE at high SNR can be expressed in terms of psi function denoted by $\psi(\cdot)$ (defined in TABLE 1) using [40, eq. (8.360/1)] as

$$\begin{aligned} \overline{SE} \approx_{\gamma \gg 1} & 1.44 \times \left(\log(\tau) + \omega \left[\log(\lambda^2 \bar{\gamma}) + 2\psi(1) \right] \right. \\ & \left. + (1-\omega) \left[\log(b^2 \bar{\gamma}) + \frac{2}{c} \psi(a) \right] \right). \end{aligned} \quad (31)$$

C. AVERAGE ENERGY EFFICIENCY

The average EE is defined as the average SE divided by the total power consumed [41]

$$\overline{EE} = \frac{\overline{SE}}{P_t + P_{diss}}, \quad (32)$$

where P_t denotes total transmit power and P_{diss} denotes power dissipation in the system's hardware components. Therefore, average EE can be calculated as

$$\overline{EE} = \frac{\overline{SE}}{P_t + p_d^s + p_d^d + n_m^2 p_d^o}, \quad (33)$$

where p_d^s, p_d^d, p_d^o denote the power dissipation at the source, receiver, and each OIRS element, respectively.

D. AVERAGE BER

In this subsection, the average BER for the proposed UWOC systems is derived. A generalized expression for BER is obtained as [42]

$$\overline{BER} = \frac{\delta}{2\Gamma(\phi)} \sum_{n=1}^N q_n^{\phi} \int_0^{\infty} \gamma^{\phi-1} \exp(-q_n\gamma) F_{\gamma}(\gamma) d\gamma, \quad (34)$$

where the parameter set $\{N, \delta, \phi, q_n\}$ vary according to the modulation and detection technique used [7]. Substituting $\exp(-q_n\gamma) = G_{0,1}^{1,0} \left[q_n\gamma \mid \begin{matrix} - \\ 0 \end{matrix} \right]$ and $F_{\gamma}(\gamma)$ from (26) in (34) and converting the Meijer's G-function into Fox-H function, we get

$$\begin{aligned} \overline{BER} = & \frac{\delta}{2\Gamma(\phi)} \sum_{n=1}^N q_n^{\phi} \int_0^{\infty} \gamma^{\phi-1} \\ & H_{0,1}^{1,0} \left[\begin{matrix} - \\ (0, 1) \end{matrix} \mid q_n\gamma \right] \left(\omega H_{1,2}^{1,1} \left[\frac{1}{\lambda} \sqrt{\frac{\gamma}{\tau\gamma}} \mid \begin{matrix} (1, 1) \\ (1, 1)(0, 1) \end{matrix} \right] \right. \\ & \left. + \frac{(1-\omega)}{2\alpha\Gamma(a)} H_{1,2}^{1,1} \left[\frac{1}{b} \sqrt{\frac{\gamma}{\tau\gamma}} \mid \begin{matrix} (1, 1) \\ (a, 1/c)(0, 1) \end{matrix} \right] \right) d\gamma. \end{aligned} \quad (35)$$

After applying [43, eq. (2.8.4)] in (35), the closed-form expression for the average BER can be expressed in terms of bivariate Fox's H function as

$$\begin{aligned} \overline{BER} = & \frac{\delta}{2\Gamma(\phi)} \sum_{n=1}^N \left(\omega H_{2,2}^{1,2} \left[\frac{1}{\lambda} \left(\frac{1}{qk\bar{\gamma}} \right)^{1/2} \mid \begin{matrix} (1, 1)(1-\phi, \frac{1}{2}) \\ (1, 1)(0, 1) \end{matrix} \right] \right. \\ & \left. + \frac{(1-\omega)}{\Gamma(a)} H_{2,2}^{1,2} \left[\frac{1}{b} \left(\frac{1}{qk\bar{\gamma}} \right)^{\frac{1}{2}} \mid \begin{matrix} (1, 1)(1-\phi, \frac{1}{2}) \\ (a, \frac{1}{c})(0, 1) \end{matrix} \right] \right). \end{aligned} \quad (36)$$

IV. NUMERICAL RESULTS

In this section, the numerical results obtained through the proposed schemes are presented and compared with the baseline scenario of NLOS-aided UWOC system. The OIRS and PMS consist of $n_m \times n_m$ mirror elements with a dimension of $l_m = 0.08$ m and $w_m = 0.08$ m. The speed of light in water (C_{water}) is assumed to be 2.25×10^8 m/sec, and the performance is demonstrated by positioning the OIRS/PMS perfectly in the middle of the transmitter and receiver when $y_s = y_d = 40$ m, if not specified otherwise. The key simulation parameters are summarized in TABLE 2. All the presented results have been obtained through Monte Carlo simulation (averaged over 10^7 channel realizations for Figs. 4, 8, and 9). MATLAB is used for calculating Meijer's G function and MATHEMATICA for Fox's H function.

A. AVERAGE SPECTRAL EFFICIENCY

When the mirror array (OIRS/PMS) of area ($a_o = 1$ m² ($n_m^2 = a_o/l_m^2 = 169$)), is fixed at a horizontal distance of 50 m from the source, i.e., $z_{kl} = 50$ m, $y_s = y_d = 40$ m, and $P_t = 43$ dBm, the plot of average SE for varying node separation (d_{sd}) is shown in Fig. 3. It can be observed from the figure that when the receiver is not directly underneath the OIRS mirror array, the average SE of OIRS is highest

TABLE 2. Simulation parameters.

Parameter	Symbol	Value
Transmit power [8]	P_t	-10 to 60 dBm
Total node separation	d_{sd}	30 m
Wavelength [2]	λ_a	532 nm
Refractive index of water [4]	μ_w	1.33643
Refractive index of air	μ_a	1
Extinction coefficient of pure seawater [44]	$c(\lambda)$	0.056 m^{-1}
Modulation parameters [7]	N, δ, ϕ, q_n	1, 1, 1/2, 1/4
Length of OIRS element	l_m	8 cm
Width of OIRS element	w_m	8 cm
Reflection efficiency of mirror element [41]	ρ	0.8
Lambertian order [41]	m	2
Depth of Transmitter	y_s	40 m
Depth of receiver	y_d	40 m
SiPM area	A_{PD}	0.0314 m^2
Optical filter gain [14]	T	1
SiPM gain [6]	G	10^6
SiPM dark current [6]	I_d	$10 \mu\text{A}$
SiPM prob. of cross-talk [6]	P_{CT}	0.03%
SiPM prob. of after pulsing [6]	P_{AP}	0.2%
SiPM excess noise factor [6]	F	1.1
Speed of light in water	C_{water}	$2.25 \times 10^8 \text{ m/sec}$
Charge on electron [6]	e	$1.6 \times 10^{-19} \text{ C}$
Transmitter inclination angles [4]	$\theta_{min}, \theta_{max}$	$0^\circ, 68^\circ$
Scintillation index [7]	σ_I^2	{0.2178, 1.9328, 3.1952}
EGG distribution parameters corresponding to different σ_I^2 [7]	$\{\omega\}_{i=1}^3$ $\{\lambda\}_{i=1}^3$ $\{a\}_{i=1}^3$ $\{b\}_{i=1}^3$ $\{c\}_{i=1}^3$	{0.1665, 0.6238, 0.7210} {0.1207, 0.1094, 0.1479} {0.1559, 0.0111, 0.0121} {1.5216, 4.4750, 7.4189} {22.8754, 105.3550, 65.6983}.
Power dissipation in transceiver [43]	$p_d^s + p_d^d$	30 dBm
Power dissipation in each OIRS element [45]	p_d^o	10 dBm

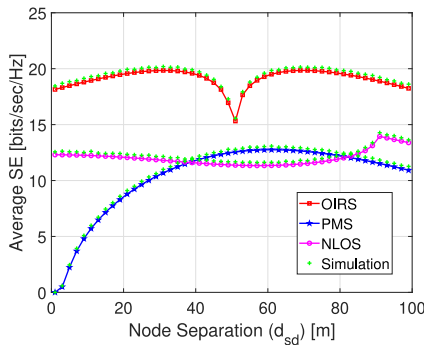


FIGURE 3. Average SE vs. node separation for different UWOC systems.

among all the scenarios. The initial increase in average SE is caused by the decrease in the total distance ($d_{sr} + d_{rd}$) between the transmitter and receiver until the receiver is just below the OIRS. The total distance then increases as the receiver moves farther away from the OIRS, lowering the total spectral efficiency. The incidence angle at the receiver is 90° when the receiver is immediately beneath the OIRS mirror array, which causes the dip in average SE of OIRS at 50.5 m, which is also evident from (5). As a consequence, it can be inferred that the receiver should not be positioned perpendicular to the OIRS. Due to the inverse relationship between the total distance ($d_{sr} + d_{rd}$) and the

received power, in a PMS scenario, the average SE initially rises and then falls as the d_{sd} increases from 1 to 100 m. There is no dip in the PMS scenario because different mirror elements have different reflection angles. Therefore, some of the rays may still reach the receiver at different angles with respect to the receiver even when it is perpendicular to the PMS. Depending on whether the incidence angle (θ_i) is smaller or greater than the critical angle (θ_c) in conventional NLOS scenario, attenuation and reflectivity play the important role. The received power signal is therefore dependent on both attenuation and reflection as $\theta_i < \theta_c$ until $d_{sd} = 90$ m. Following this point, $\theta_i > \theta_c$ and hence the total received power solely depends on the attenuation factor, which is also evident from (17). Furthermore, it can be observed that conventional NLOS-assisted UWOC systems outperform PMS-assisted systems under certain conditions, such as when the receiver is close to the transmitter or when θ_i exceeds θ_c , but this scheme is not applicable for deep sea application scenarios since optical signal transmission underwater is limited to a few tens of meters.

Fig. 4 shows the results for the average SE of the three scenarios with regard to the transmit power (P_t) utilizing EGG distribution for various scintillation indices (σ_I^2) of 0.2178, 1.9328, and 3.1952. The corresponding values of ω , λ , a , b , and c for these scintillation indices are given in TABLE 2. It is assumed that the OIRS/PMS is positioned

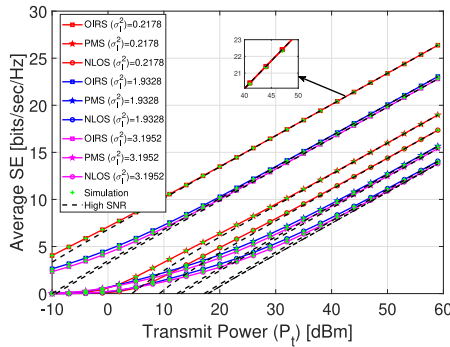


FIGURE 4. Average SE vs. transmit power for different UWOC systems.

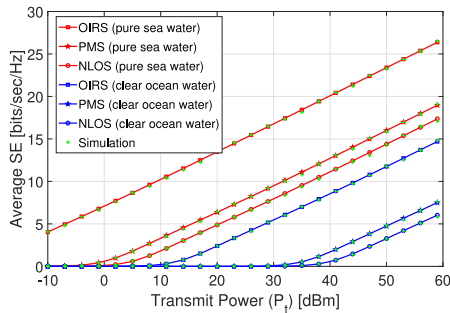


FIGURE 5. Average SE vs. transmit power for different water types.

15 m away from the transmitter and $d_{sd} = 30$ m. From Fig. 4, it can be observed that the proposed OIRS-assisted UWOC scenario outperforms the PMS and NLOS-assisted UWOC systems. Additionally, in all three circumstances, the average SE decreases with a large scintillation index (strong turbulence), as expected. Furthermore, the PMS-assisted UWOC system performs better than the NLOS-assisted UWOC system. This is because some part of the signal in the NLOS-assisted UWOC system is lost into the air at the water-air interface, but there is no such loss in PMS case. As a result, it can be inferred that the proposed UWOC systems perform better than the benchmark case in terms of SE.

In Fig. 5, the average SE is plotted for two different water types which include pure sea water and clear ocean water, when $\sigma_I^2 = 0.2178$. The results demonstrate that the average SE of pure sea water is higher than that of clear ocean water. This is due to the fact that clear ocean water has a higher attenuation coefficient ($c(\lambda)$) of 0.151 than pure sea water with $c(\lambda) = 0.056$ [3].

Fig. 6 depicts the average SE when the transmitter depth (y_s) is varied from 1 m to 60 m. It is assumed that the receiver is positioned at a depth of 20 m from the water-air interface, and z_{kl} is 15 m. a_o is assumed to be 1 m^2 . It can be observed from Fig. 5 that the average SE is low when the source is close (y_s is 1m to 7 m) to the reflector plane (water-air interface). This attributes to large incidence angle at the OIRS plane and consequently small received power at the receiver. This owes to the principle of operation of the mirror array reflector in which it is assumed that the

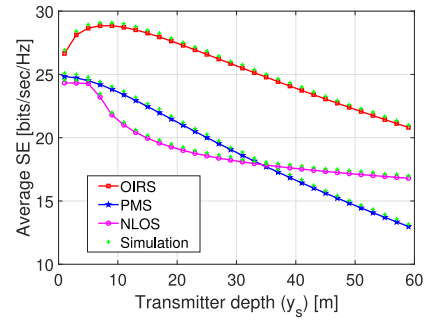


FIGURE 6. Average SE vs. transmitter depth for different UWOC systems.

TABLE 3. Incidence angle (θ_i) for varying transmitter depths (y_s).

Transmitter depth (y_s) [m]	Incidence angle (θ_i)
1	55.0079
2	53.7461
5	50.1944
6	49.0856
7	$48.0127 < \theta_c$

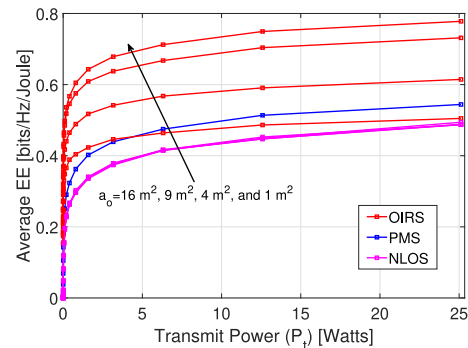


FIGURE 7. Average EE vs. transmit power for different UWOC systems.

reflecting element's two rotational degrees of freedom lie between $[-\pi/2, \pi/2]$. The reduction in the average SE is due to increased pathloss with increase in total distance between the transmitter and the receiver, when $y_s > 7$ m. The converse scenario for OIRS, when the source is considered to be fixed and the receiver depth (y_d) is variable, also exhibits a similar pattern of behaviour. In the case of PMS, as the signal from all of the PMS elements doesn't fall on the receiver FOV, so its average SE is less than that of the OIRS scenario. In the NLOS scenario, the average SE is initially high until $y_s = 7$ m; the reason behind this high SE is the TIR occurring at the water-air interface as θ_i is more than the $\theta_c = 48.4401$. After $y_s = 7$ m, as $\theta_i < \theta_c$, therefore the average SE reduces as a function of both pathloss and reflectivity. TABLE 3 shows the values of incidence angle for various transmitter depths.

B. AVERAGE ENERGY EFFICIENCY

Fig. 7 shows the plot of average EE result with respect to the transmit power (in watts) for varying a_o , assuming $p_d^s + p_d^d = 30$ dBm, and $p_d^o = 10$ dBm. There are a total of 156, 625, 1406, and 2500 OIRS elements that corresponds to $a_o = 1 \text{ m}^2, 4 \text{ m}^2, 9 \text{ m}^2,$ and 16 m^2 , respectively. It is

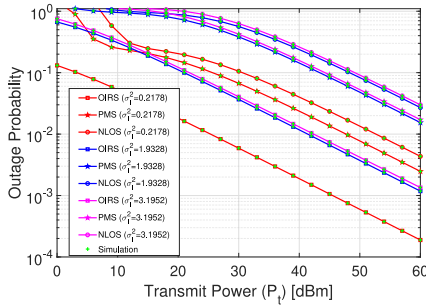


FIGURE 8. Outage probability vs. transmit power for different UWOC systems.

observed that the average EE decreases as the OIRS area or the number of reflecting elements increases. This is due to the fact that the average SE reaches saturation for large number of reflecting elements, whereas energy consumption increases linearly with increasing n_m . Since no power is required by the PMS elements for reflecting the signal in PMS-assisted UWOC scenarios, the EE will not reduce by increasing the number of reflecting elements. It is therefore, concluded that expanding the area of OIRS result in a decreased EE. This is due to the fact that increasing the OIRS area increases circuit power consumption, whereas the SE saturates after a small initial rise with increase in OIRS area. As a result of this compounding effect, the EE for a large number of reflecting elements decreases. This can also be observed analytically from (33).

C. OUTAGE PROBABILITY

Next, the outage probability performance of the proposed UWOC systems under varying turbulence effects is presented in Fig. 8, when $\gamma_{th} = 4$ dB. It is assumed that $d_{sd} = 30$ m, and the OIRS is placed exactly in the middle of the transmitter and the receiver. Additionally, a_o is assumed to be 1 m^2 . From Fig. 8, the following observations can be made: a) OIRS-assisted UWOC system shows a significant improvement in the outage probability in all three turbulence scenarios (strong, moderate, and weak), b) increasing σ_I^2 , increases the outage probability as can be observed from the plots of OIRS for $\sigma_I^2 = 0.2178, 1.9328,$ and $3.1952,$ and c) the outage probability of OIRS-assisted UWOC system is 1.8×10^{-4} at transmit power of 60 dBm, whereas at the same amount of transmit power, the outage probability of PMS and NLOS-assisted UWOC systems is 2.4×10^{-3} and $4.34 \times 10^{-3},$ respectively when $\sigma_I^2 = 0.2178.$

The outage probability versus transmit power performance of the proposed OIRS-assisted UWOC systems for different γ_{th} is presented in Fig. 9. From the figure, it is clearly seen that the outage probability increases as predicted when γ_{th} increases.

D. AVERAGE BER

Finally, in Fig. 10, the average BER for IM/DD with OOK is plotted against transmit power (P_t) for various channel conditions varying from weak to strong turbulence. This

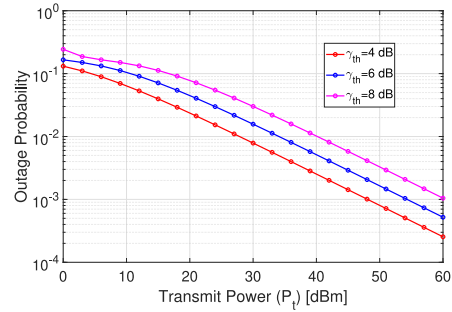


FIGURE 9. Outage probability vs. transmit power considering OIRS-assisted UWOC system for different SNR threshold (γ_{th}).

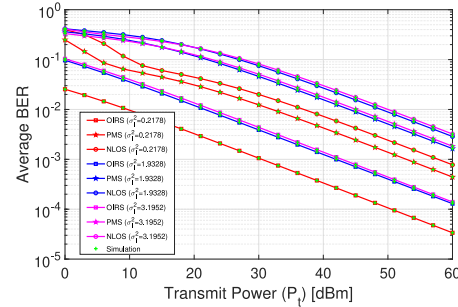


FIGURE 10. Average BER vs. transmit power for different UWOC systems.

average BER plot shows similar kind of observations as the outage probability does. It is observed from this plot that the OIRS shows improved average BER, followed by PMS and NLOS. For example, BER of OIRS, PMS, and NLOS is $3.37 \times 10^{-5}, 4.42 \times 10^{-4},$ and $7.76 \times 10^{-4},$ respectively, at $P_t = 60$ dBm for $\sigma_I^2 = 0.2178.$ Also, it can be observed from Fig. 10 that as the scintillation index value becomes higher, it result in an increase in the average BER. The average BER of NLOS-assisted UWOC system with the weak turbulence ($\sigma_I^2 = 0.2178$) and strong turbulence ($\sigma_I^2 = 3.1952$) is $7.76 \times 10^{-4},$ and $3.21 \times 10^{-3},$ respectively. Hence it is obvious that the OIRS-assisted UWOC system is more reliable than PMS and NLOS UWOC systems.

V. CONCLUSION AND FUTURE WORK

In this work, two NLOS UWOC methods employing mirror-based OIRS and PMS are proposed and compared to the conventional TIR based NLOS methodology for UWOC systems in the literature. Specifically, the average SE, average EE, outage probability, and average BER is analyzed by deriving the closed-form expressions of these proposed systems. The findings demonstrate a considerable performance improvement using the proposed OIRS-assisted UWOC system. Additionally, the efficient zones of OIRS deployments are analyzed and the results show an interesting observation that the OIRS should not be placed very close (at 90°) to transmitter or receiver. Moreover, the transmitter/receiver should not be placed very close to the OIRS plane. Furthermore, conventional NLOS-assisted UWOC systems and PMS UWOC systems show a comparable

performance. This work can be extended in future by analyzing the performance studies that take into account the effect of wind and ocean currents on the orientation and displacement of the transmitter, the OIRS/PMS, and the receiver. Additionally, a hybrid acoustic-UWOC system with OIRS may be one of the future extensions of this study. In the current work, an OIRS is serving a single receiver. The same OIRS can be used to serve multiple receivers (i.e., OIRS with NOMA), which can be another option for future work.

APPENDIX A PROOF OF LEMMA 1

For any random variable z , the PDF can be obtained by using inverse mellin transform as

$$f_Z(z) = \frac{1}{2\pi iz} \int_{\zeta-i\infty}^{\zeta+i\infty} z^{-n} \mathbb{E}[Z^n] dn, \quad (37)$$

where $\zeta - i\infty$ to $\zeta + i\infty$ denotes the line integral, $\mathbb{E}[\cdot]$ denotes the expectation operator and $\mathbb{E}[X^n]$ denotes the n^{th} order moment. The n^{th} order moment of h_α is expressed as

$$\mathbb{E}[h_\alpha^n] = \int_0^\infty h_\alpha^n f_{h_\alpha}(h_\alpha) dh_\alpha. \quad (38)$$

Now substituting (4) in (38) and then using [40, eqs. (3.351/3) and (3.478/1)], we get

$$\mathbb{E}[h_\alpha^n] = \left(\omega \lambda^n \Gamma(1+n) + \frac{(1-\omega)b^n \Gamma(a+n/c)}{\Gamma(a)} \right). \quad (39)$$

Now using (39) in (37) and then using the definition of Fox-H function to get $f_{h_\alpha}(h_\alpha)$ in (23), which concludes the proof of Lemma 1.

APPENDIX B PROOF OF LEMMA 2

The CDF of γ , which is related to PDF by the relation as $F_\gamma(\bar{\gamma}) = \int_0^{\bar{\gamma}} f_\gamma(\bar{\gamma}) d\bar{\gamma}$ can be obtained by using (25) and solving the inner integral as

$$\int_0^\gamma \gamma^{-\frac{n}{2}-1} d\gamma = -\frac{\gamma^{-\frac{n}{2}}}{-\frac{n}{2}} = \gamma^{-\frac{n}{2}} \frac{\Gamma(n)}{\Gamma(1-n)},$$

then using the definition of Meijer's G function in [43, eq. (2.9.1)], and then converting it to Fox's H function yields the CDF of SNR in (26), which concludes the proof of Lemma 2.

REFERENCES

- [1] M. Jain, N. Sharma, A. Gupta, D. Rawal, and P. Garg, "NOMA assisted underwater visible light communication system with full-duplex cooperative relaying," *Veh. Commun.*, vol. 31, Oct. 2021, Art. no. 100359.
- [2] H. Kaushal and G. Kaddoum, "Underwater optical wireless communication," *IEEE Access*, vol. 4, pp. 1518–1547, 2016.
- [3] Z. Zeng, S. Fu, H. Zhang, Y. Dong, and J. Cheng, "A survey of underwater optical wireless communications," *IEEE Commun. Surveys Tuts.*, vol. 19, no. 1, pp. 204–238, 1st Quart., 2017.
- [4] S. Arnon and D. Kedar, "Non-line-of-sight underwater optical wireless communication network," *J. Opt. Soc. Amer. A Opt. Image Sci.*, vol. 26, no. 3, pp. 530–539, 2009.
- [5] N. Anous, M. Abdallah, M. Uysal, and K. Qaraqe, "Performance evaluation of LOS and NLOS vertical inhomogeneous links in underwater visible light communications," *IEEE Access*, vol. 6, pp. 22408–22420, 2018.
- [6] I. C. Ijeh, M. A. Khalighi, and S. Hranilovic, "Parameter optimization for an underwater optical wireless vertical link subject to link misalignments," *IEEE J. Ocean. Eng.*, vol. 46, no. 4, pp. 1424–1437, Oct. 2021.
- [7] E. Zedini, H. M. Oubei, A. Kammoun, M. Hamdi, B. S. Ooi, and M.-S. Alouini, "Unified statistical channel model for turbulence-induced fading in underwater wireless optical communication systems," *IEEE Trans. Commun.*, vol. 67, no. 4, pp. 2893–2907, Apr. 2019.
- [8] Z. Rahman, N. V. Tailor, S. M. Zafaruddin, and V. K. Chaubey, "Unified performance assessment of optical wireless communication over multi-layer underwater channels," *IEEE Photon. J.*, vol. 14, no. 5, pp. 1–14, Oct. 2022.
- [9] X.-H. Huang et al., "6-m/10-Gbps underwater wireless red-light LASER transmission system," *Opt. Eng.*, vol. 57, no. 6, 2018, Art. no. 66110.
- [10] F. C. Okogbaa et al., "Design and application of intelligent reflecting surface (IRS) for beyond 5G wireless networks: A review," *Sensors*, vol. 22, no. 7, p. 2436, 2022.
- [11] V. Jamali, H. Ajam, M. Najafi, B. Schmauss, R. Schober, and H. V. Poor, "Intelligent reflecting surface assisted free-space optical communications," *IEEE Commun. Mag.*, vol. 59, no. 10, pp. 57–63, Oct. 2021.
- [12] M. D. Renzo et al., "Smart radio environments empowered by reconfigurable AI Meta-surfaces: An idea whose time has come," *EURASIP J. Wireless Commun. Netw.*, vol. 2019, no. 1, pp. 1–20, 2019.
- [13] S. Aboagye, A. R. Ndjiongue, T. Ngatched, O. Dobre, and H. V. Poor, "RIS-assisted visible light communication systems: A tutorial," 2022, *arXiv:2204.07198*.
- [14] S. Aboagye, T. M. N. Ngatched, O. A. Dobre, and A. R. Ndjiongue, "Intelligent reflecting surface-aided indoor visible light communication systems," *IEEE Commun. Lett.*, vol. 25, no. 12, pp. 3913–3917, Dec. 2021.
- [15] Q. Wu, S. Zhang, B. Zheng, C. You, and R. Zhang, "Intelligent reflecting surface-aided wireless communications: A tutorial," *IEEE Trans. Commun.*, vol. 69, no. 5, pp. 3313–3351, May 2021.
- [16] S. Liu, L. Xiao, M. Zhao, X. Xu, and Y. Li, "Performance analysis of intelligent reflecting surface in multi-user MIMO systems," *J. Phys. Conf.*, vol. 1575, no. 1, 2020, Art. no. 12078.
- [17] J. Chen, Y.-C. Liang, Y. Pei, and H. Guo, "Intelligent reflecting surface: A programmable wireless environment for physical layer security," *IEEE Access*, vol. 7, pp. 82599–82612, 2019.
- [18] M. Najafi and R. Schober, "Intelligent reflecting surfaces for free space optical communications," in *Proc. IEEE Global Commun. Conf. (GLOBECOM)*, 2019, pp. 1–7.
- [19] E. Björnson, Ö. Özdogan, and E. G. Larsson, "Intelligent reflecting surface versus decode-and-forward: How large surfaces are needed to beat relaying?" *IEEE Wireless Commun. Lett.*, vol. 9, no. 2, pp. 244–248, Feb. 2020.
- [20] M. H. N. Shaikh, V. A. Bohara, A. Srivastava, and G. Ghatak, "Intelligent reflecting surfaces versus full-duplex relaying: Performance comparison for non-ideal transmitter case," in *Proc. IEEE 32nd Annu. Int. Symp. Pers. Indoor Mobile Radio Commun. (PIMRC)*, 2021, pp. 513–518.
- [21] L. Yang, Q. Zhu, S. Li, I. S. Ansari, and S. Yu, "On the performance of mixed FSO-UWOC dual-hop transmission systems," *IEEE Wireless Commun. Lett.*, vol. 10, no. 9, pp. 2041–2045, Sep. 2021.
- [22] S. Li, L. Yang, D. B. D. Costa, M. D. Renzo, and M.-S. Alouini, "On the performance of RIS-assisted dual-hop mixed RF-UWOC systems," *IEEE Trans. Cogn. Commun. Netw.*, vol. 7, no. 2, pp. 340–353, Jun. 2021.
- [23] L. B. Kumar, R. P. Naik, P. Krishnan, A. A. B. Raj, A. K. Majumdar, and W.-Y. Chung, "RIS assisted triple-hop RF-FSO convergent with UWOC system," *IEEE Access*, vol. 10, pp. 66564–66575, 2022.
- [24] M. Elsayed, A. Samir, A. A. A. El-Banna, W. U. Khan, S. Chatzinotas, and B. M. ElHalawany, "Mixed RIS-relay NOMA-based RF-UWOC systems," in *Proc. IEEE 95th Veh. Technol. Conf. (VTC-Spring)*, 2022, pp. 1–6.

- [25] L. B. Kumar, P. N. Ramavath, P. Krishnan, and A. K. Majumdar, "Underwater wireless optical communications based reconfigurable UOWSN for monitoring and discovering continental margin ore deposits," *Appl. Opt.*, vol. 61, no. 11, pp. 3141–3149, 2022.
- [26] S. A. H. Mohsan, A. Mazinani, N. Q. H. Othman, and H. Amjad, "Towards the Internet of Underwater Things: A comprehensive survey," *Earth Sci. Inform.*, vol. 15, pp. 735–764, Mar. 2022.
- [27] S. Kisseleff, S. Chatzinotas, and B. Ottersten, "Reconfigurable intelligent surfaces in challenging environments: Underwater, underground, industrial and disaster," *IEEE Access*, vol. 9, pp. 150214–150233, 2021.
- [28] Z. Tian et al., "Programmable acoustic metasurfaces," *Adv. Funct. Mater.*, vol. 29, no. 13, 2019, Art. no. 1808489.
- [29] Z. Sun, H. Guo, and I. F. Akyildiz, "High-data-rate long-range underwater communications via acoustic reconfigurable intelligent surfaces," *IEEE Commun. Mag.*, vol. 60, no. 10, pp. 96–102, Oct. 2022.
- [30] R. P. Naik and W.-Y. Chung, "Evaluation of reconfigurable intelligent surface-assisted underwater wireless optical communication system," *J. Lightw. Technol.*, vol. 40, no. 13, pp. 4257–4267, Jul. 1, 2022.
- [31] Y. Ata, H. Abumarshoud, L. Bariah, S. Muhaidat, and M. A. Imran, "Intelligent reflecting surfaces for underwater visible light communications," *IEEE Photon. J.*, vol. 15, no. 1, pp. 1–10, Feb. 2023.
- [32] A. M. Abdelhady, A. K. S. Salem, O. Amin, B. Shihada, and M.-S. Alouini, "Visible light communications via intelligent reflecting surfaces: Metasurfaces vs mirror arrays," *IEEE Open J. Commun. Soc.*, vol. 2, pp. 1–20, 2021.
- [33] M.-A. Khalighi, T. Hamza, S. Bourennane, P. Léon, and J. Opderbecke, "Underwater wireless optical communications using silicon photomultipliers," *IEEE Photon. J.*, vol. 9, no. 4, pp. 1–10, Aug. 2017.
- [34] E. Sarbazi, M. Safari, and H. Haas, "Statistical modeling of single-photon avalanche diode receivers for optical wireless communications," *IEEE Trans. Commun.*, vol. 66, no. 9, pp. 4043–4058, Sep. 2018.
- [35] N. Saeed, A. Celik, T. Y. Al-Naffouri, and M.-S. Alouini, "Underwater optical wireless communications, networking, and localization: A survey," *Ad Hoc Netw.*, vol. 94, Nov. 2019, Art. no. 101935.
- [36] F. Miramirkhani and M. Uysal, "Visible light communication channel modeling for underwater environments with blocking and shadowing," *IEEE Access*, vol. 6, pp. 1082–1090, 2018.
- [37] H. E. Nistazakis, E. A. Karagianni, A. D. Tsigopoulos, M. E. Fafalios, and G. S. Tombras, "Average capacity of optical wireless communication systems over atmospheric turbulence channels," *J. Lightw. Technol.*, vol. 27, no. 8, pp. 974–979, Apr. 2009.
- [38] A. Lapidoth, S. M. Moser, and M. A. Wigger, "On the capacity of free-space optical intensity channels," *IEEE Trans. Inf. Theory*, vol. 55, no. 10, pp. 4449–4461, Oct. 2009.
- [39] Y. B. A. Prudnikov and O. Marichev, *Integrals and Series: More Special Functions*. Boca Raton, FL, USA: CRC Press, 1999.
- [40] I. S. Gradshteyn and I. M. Ryzhik, *Table of Integrals, Series and Products*. New York, NY, USA: Academic, 2000.
- [41] L. Zhan, H. Zhao, W. Zhang, and J. Lin, "An optimal scheme for the number of mirrors in vehicular visible light communication via mirror array-based intelligent reflecting surfaces," *Photonics*, vol. 9, no. 3, p. 129, 2022.
- [42] E. Zedini, H. Soury, and M.-S. Alouini, "Dual-hop FSO transmission systems over gamma-gamma turbulence with pointing errors," *IEEE Trans. Wireless Commun.*, vol. 16, no. 2, pp. 784–796, Feb. 2017.
- [43] A. Kilbas and M. Saigo, *H-Transforms: Theory and Applications (Analytical Methods and Special Functions)*. 1st ed. Boca Raton, FL, USA: CRC Press, 2004.
- [44] M. F. Ali, D. N. K. Jayakody, Y. A. Chursin, S. Affes, and S. Dmitry, "Recent advances and future directions on underwater wireless communications," *Arch. Comput. Methods Eng.*, vol. 27, no. 5, pp. 1379–1412, 2020.
- [45] C. Huang, A. Zappone, G. C. Alexandropoulos, M. Debbah, and C. Yuen, "Reconfigurable intelligent surfaces for energy efficiency in wireless communication," *IEEE Trans. Wireless Commun.*, vol. 18, no. 8, pp. 4157–4170, Aug. 2019.